

Helios 2.0: A Robust, Ultra-Low Power Gesture Recognition System Optimised for Event-Sensor based Wearables

Prarthana Bhattacharyya* Joshua Mitton* Ryan Page* Owen Morgan* Oliver Powell*
 Benjamin Menzies Gabriel Homewood Kemi Jacobs Paolo Baesso Taru Muhonen
 Richard Vigars Louis Berridge
 Ultraleap Ltd., Glass Wharf, Bristol, UK

{prarthana.bhattacharyya, ryan.page, owen.morgan, oliver.powell}@ultraleap.com

Abstract

We present an advance in wearable technology: a mobile-optimized, real-time, ultra-low-power event camera system that enables natural hand gesture control for smart glasses, dramatically improving user experience. While hand gesture recognition in computer vision has advanced significantly, critical challenges remain in creating systems that are intuitive, adaptable across diverse users and environments, and energy-efficient enough for practical wearable applications. Our approach tackles these challenges through carefully selected microgestures: lateral thumb swipes across the index finger (in both directions) and a double pinch between thumb and index fingertips. These human-centered interactions leverage natural hand movements, ensuring intuitive usability without requiring users to learn complex command sequences. To overcome variability in users and environments, we developed a novel simulation methodology that enables comprehensive domain sampling without extensive real-world data collection. Our power-optimised architecture maintains exceptional performance, achieving F1 scores above 80% on benchmark datasets featuring diverse users and environments. The resulting models operate at just 6-8 mW when exploiting the Qualcomm Snapdragon Hexagon DSP, with our 2-channel implementation exceeding 70% F1 accuracy and our 6-channel model surpassing 80% F1 accuracy across all gesture classes in user studies. These results were achieved using only synthetic training data. This improves on the state-of-the-art for F1 accuracy by 20% with a power reduction 25x when using DSP. This advancement brings deploying ultra-low-power vision systems in wearable devices closer and opens new possibilities for seamless human-computer interaction. A real-time video demonstration of Helios 2.0 can be found [at this link](#).

*Equal contribution



Figure 1. Our system enables natural hand gesture interaction with smart glasses without requiring additional peripherals. The event-based vision approach allows for low-power, responsive gesture recognition even in challenging lighting conditions.

1. Introduction

Hand gestures represent one of the most natural human-computer interaction paradigms, offering intuitive control without requiring visual attention from the user. As the number of smart glass devices has exploded over the last year, highlighted by their emergence as a wearable product category at the Consumer Electronics Show (CES) 2025, efficient gesture interaction has become increasingly important. Currently, these devices almost exclusively use capacitive touch on the glasses’ temple for their human-machine interface — a solution that is often awkward to use, limits interaction vocabulary, and can be socially conspicuous as users repeatedly reach to touch their eyewear. The industry has acknowledged these limitations by introducing additional peripherals, such as rings or wrist bands. While these accessories enable more intuitive and ergonomic hand-based input, they require users to wear and maintain an additional piece of hardware. To overcome this need for additional devices while still leveraging natural hand-based input, an event-based vision system was previously proposed [5]. In this work, we present signif-

icant improvements to the event-based gesture recognition approach in three key areas: (1) enhanced simulation methodology, (2) redesigned model architecture optimised for mobile deployment, and (3) comprehensive testing benchmarks across varied users and environments. These improvements result in a model that achieves F1 accuracy greater than 70% for 2-channel models and greater than 80% for 6-channel models across multiple users and environments, while only consuming 6-7 mW when running computationally intensive portions on a Qualcomm Snapdragon Hexagon DSP. The model is specifically designed for low-power operation and is composed of five stages, with two stages containing the majority of the computational burden running on the DSP. With a model latency of 2.34 ms, the system enables smooth and responsive interaction that feels natural to users. These advances make hand gesture interaction with smart glasses more accessible, eliminating the need for additional accessories while maintaining a socially acceptable and power-efficient interaction paradigm. The rest of the paper breaks down the specific enhancements made to the system and presents comprehensive evaluation results, before concluding with future directions for this technology.

2. Related Work

While our work is the first to propose an ultra-low-power solution for natural hand interactions on smart glass devices, it builds upon prior research in gesture recognition, machine learning for event-based vision, and low-bit quantisation for efficient inference. Below are the key works, the reader is referred to the supplementary material for a more complete overview.

2.1. Hand gesture recognition

Hand Gesture Recognition (HGR) has been explored across various sensing modalities [16, 41]. Data gloves [12] provide high accuracy but are unsuitable for continuous use. Vision-based methods using traditional cameras [3, 24, 29, 48, 61] combined with deep learning models [18, 22, 32, 33, 37, 49] demonstrate strong performance in controlled environments but struggle with environmental variations and computational constraints. Previous work [9] reduced frame rates and employed standby modes to save power to achieve real-time gesture recognition but faced a fundamental tradeoff, lower latency requires higher sampling rates leading to increased power consumption. Alternative approaches like sEMG [30] and ultrasound [59] offer unique advantages but face challenges with electrode placement, muscle fatigue, or specialised hardware requirements.

2.2. Event Representations and ML Architectures

Event cameras produce sparse, asynchronous data unlike traditional synchronous, dense images [13], necessitating specialised representations and architectures. Quantisation



Figure 2. Hardware used for data collection and model testing. The event-camera is mounted on the left side of the glasses, with the display connection on the right.

techniques reduce neural network latency and power consumption by storing weights and activation tensors in lower bit precision [36, 52, 58]. Post-Training Quantisation (PTQ) [47] quantises pre-trained models with minimal engineering effort, while Quantisation-Aware Training (QAT) [17] incorporates simulated quantisation during training to better preserve accuracy, especially for low-bit quantisation. In our work, we develop a QAT-scheme for our custom architecture to significantly reduce power consumption without sacrificing gesture recognition accuracy. Unlike Meta’s approach [21], which relies on frame-based cameras and hand skeletal tracking, our method eliminates the need for explicit hand pose estimation by directly recognising gestures from raw event streams. The most closely related work [2] also utilises event-based gesture recognition but employs the DVS-128 camera, which is impractical for integration with smart eyewear. Additionally, we address the critical challenge of false positives from ego-motion by explicitly modeling adversarial classes alongside relevant microgestures, a concern not actively mitigated in prior works [1, 2, 21].

3. Hardware

This section details our test platform and power measurement setup.

3.1. Test Platform

Our system uses a Prophesee GenX320 event camera with a custom USB readout PCB, based on [5]. The key differences are where the camera was mounted and execution hardware. We mounted the event camera on XReal Airs to enable richer visual experiences and user testing. Fig. 2 shows this configuration, with the event camera and USB readout on the temple, alongside the XReal’s display connection. Both connect to a USB hub linked to an Android phone.

For mobile-optimised model development, we used an Android OnePlus 10 Pro with the Qualcomm Snapdragon 8

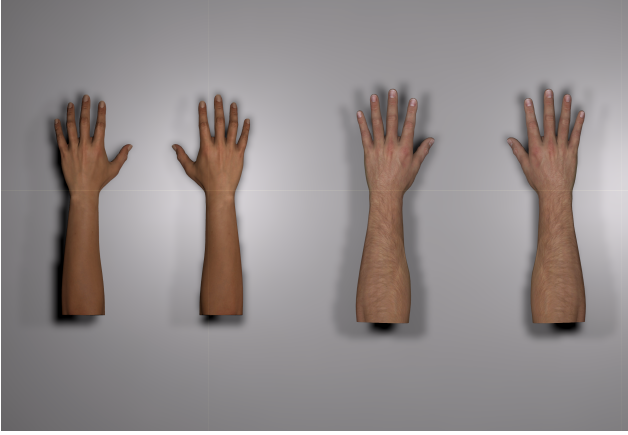


Figure 3. Examples of the 3D hand models used for simulation.

Gen1, featuring Hexagon DSP for acceleration. While this offers more computing power than in [5], it provided insights into how DSP and NPUs would enhance model performance in future smart glass products.

3.2. Model Power Evaluation

To determine the model power consumption a Snapdragon XR2Gen2 based platform was used. The CPU architecture is similar to the Snapdragon 8 Gen1 featuring Kryo Prime, Gold and Silver ARM based CPU cores and Hexagon DSP [57]. The power was calculated by measuring the current consumption using a 16-bit ADC that sampled the voltage across a shunt resistor in series with the device. This was multiplied by the input voltage provided by a dedicated PSU, also sampled by a 16-bit ADC, to give the total device power. To calculate the power used by the model, the following test sequence is carried out using a test harness: first the harness loads the input data for testing and runs all base tasks, except for model execution, recording the power P_{base} . On the next run, the harness runs and loads the same data, but this time completes N iterations of the model over it. The test harness then terminates the measurement, logging the total power of the run, P_{total} . It should be noted the data is from a user recording, so it is representative of what the model would process at inference time. Finally, the power consumption of the model P_{model} was calculated using the following $P_{model} = (P_{total} - P_{base})/N$.

4. Datasets

4.1. Synthetic Datasets

This section explains our simulation-based approach to dataset generation. By combining eSIM’s event generation capabilities [42] with a custom Unity-powered [54] rendering engine, the system synthesises realistic hand gesture events for training purposes.



Figure 4. Examples of the 3D environments used within simulation.

4.1.1. Simulator Details

The simulator leverages Ultraleap’s *Orion* [53] hand tracking data, recorded at 90 Hz and segmented into 40-frame sequences to enable simulation-time augmentation. Pre-processing includes balancing left/right hand chiralities through mirroring, removing poor poses and sequences with multiple consecutive untracked frames, and filling single missing frames via linear interpolation to prevent rendering artifacts. The processed data drives hand mesh rigging (Fig. 3) within Unity’s High Definition Render Pipeline, which renders photorealistic hands in synthetic 3D environments (Fig. 4).

4.1.2. Simulator Augmentation

Simulator augmentations fall into three categories: (1) environment modifications including lighting and hand positioning, (2) random mutation of recorded data, and (3) formation of hand data into Helios 2.0 micro gesture classes.

Environmental augmentations include varying scene lighting brightness (50-400% of nominal values) while maintaining fixed camera exposure. Camera movement follows a pathfinding algorithm that navigates between “safe” zones on the (x, y) ground plane while continuously rotating around its yaw axis to simulate head motion typical of head-mounted AR glasses.

For data augmentation, we reconstruct a forward kinematic model of bone angles and apply small random continuous deviations each frame, ensuring unique data generation in each simulation run. Micro gesture class construction is detailed in the following section.

4.1.3. Longer Sequences

In [5], a 7-class model was proposed with gestures comprising unknown motions, untracked hands, pinch, double pinch, swipe left, swipe right, and rest positions, generated in a single time window of 434 ms. In Helios 2.0, to improve system robustness, we extended sequence length from 434ms to 2s and expanded from 7 to 10 classes by adding “return” versions of several gestures. The expanded classification includes: Unknown, Untracked,



Figure 5. Left to right, pinch, left swipe, right swipe, with the end point of the gesture illustrated on the bottom.

Pinch, Double Pinch, Pinch (return), Swipe Left, Swipe Left (return), Swipe Right, Swipe Right (return), and Rest. Fig. 5 illustrates swipe and pinch gestures in the simulator.

Our animation approach uses forward kinematics with motion derived from Optitrack user studies, which revealed gesture motions approximating sigmoid curves $S(x) = \frac{1}{1 + e^{-mx}}$. We implemented four sigmoid variations for dataset diversity.

This combined with gesture expansion explicitly addresses false positives—for example, when returning to rest position after a right swipe, the leftward motion might incorrectly trigger a left swipe, causing user frustration in menu navigation scenarios.

We redefined each gesture to approximately 333ms, allowing six different gestures within a 2s sequence. Rather than random selection, we implemented structured transition rules between gestures as a Markov chain, with rest position serving as a root state. For class balance, we manually weighted probabilities (Fig. 6) rather than using algorithmic approaches like Reverse Page Rank [4]. Between certain transitions (rest to swipe, rest to unknown, or rest to pinch), we apply frame blending through linear interpolation in angle space to ensure kinematically plausible motions.

4.1.4. Rendering and Event Generation

After mutating hand positions, we render frames and then generate events utilising an Unity implementation of eSIM [42], where an event is given by $P_i := (x_i, y_i, p_i, t_i)$ where x_i, y_i are the (x, y) pixel coordinates respectively, p_i is the polarity defined as 1 for positive changes and 0 for negative changes and t_i is the time the event occurred, in ns for event i . To ensure contrast detection is possible across the scene, we employ High Dynamic Range (HDR) rendering to prevent event loss in regions that saturate in the 8-bit range

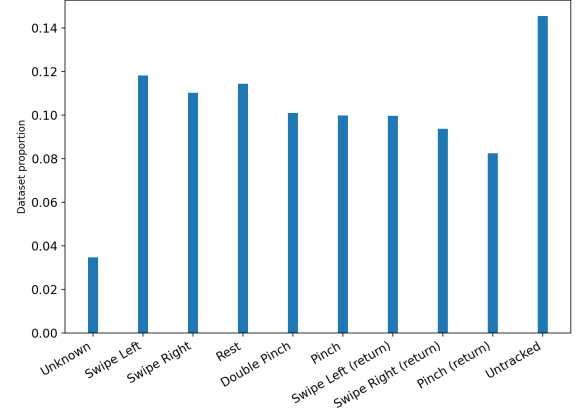


Figure 6. Distribution of classes from a subset of the training data.

(0-255). This accommodates more diverse environmental and lighting variations, closer to real-world scenarios. The Simulation outputs both events, current active gesture and 3D hand joint location at 900Hz rather than the input data’s 90Hz for precise event timing. The following section describes how the event stream is processed before being used to train models.

4.1.5. Event Representation

Following [5], we use polarity-separated event Time Surfaces (TS) as our event representation for training. We build on the Locally-Normalised Event Surfaces (LNES) approach from [45]. To construct the TS representation $\mathcal{I}_k \in \mathbb{R}^{w \times h \times 2}$, we divide an event stream of length L into discrete time windows. In our longer-sequence datasets, we set $L = 2$ s, which is split into 25 time steps of 80 ms each. Thus, $k \in \{0, 1, \dots, 24\}$ indexes each of these 25 windows. We denote the duration of each time window by T_s . \mathcal{I}_k is created by first initialising it with zeros and collecting events that have incoming timestamps T_i within this window by iterating through from the oldest to the newest event. We reduced T_s from 433ms to 240ms to improve temporal consistency for shorter gestures in longer windows. To create LNES, we initialise the TS \mathcal{I}_k to zeros and update pixel values with an exponential decay:

$$\mathcal{I}_k = \begin{cases} -\lambda \left(\frac{T_{max} - T_i}{T_s} \right), & \text{if } T_{max} - T_i < T_s \\ 0, & \text{otherwise} \end{cases} \quad (1)$$

Where T_{max} is the maximum timestamp in the window, $\lambda = 5$ is the decay constant, and T_i is the timestamp of the incoming event. During inference, pixels with timestamps older than T_s are reset to zero.

For an event stream with image bounds $\{w, h\}$, we accumulate positive polarity events in the range $\{w, h\}$ and negative polarity events in the range $\{w, 2h\}$, thereby reshaping $\mathcal{I}_k \in \mathbb{R}^{w \times 2h}$ (Fig. 7 - note for illustration purposes Figure 7



Figure 7. Example time surface with left hand side illustrating the positive polarity image and right hand side illustrating the negative polarity image.

displays the image as $\{2w, h\}$.

The 3D hand joint locations are reprojected into 2D camera space to obtain bounding box locations. Points beyond image bounds are clipped to $\{[0, w-1], [0, h-1]\}$. Bounding box corners are computed via min-max operations, excluding points below the wrist for better box tightness. As an improvement on prior work, we enforce square bounding boxes for improved training accuracy and reduced sim-to-real gap at inference time.

4.2. Real Dataset Curation

We developed an Android testing application to collect gesture data for model benchmarking. The app captured user experience level, personal characteristics (hand size, skin tone using the Monk Skin Tone Scale), and environmental factors (lighting, motion status). The tests consisted of 60 trials where users performed random prompted gestures (pinch, left/right swipe) without visual feedback to prevent behaviour modification. Each trial logged the requested gesture, timing information, and raw event stream data for subsequent analysis. For further details including images, readers are referred to the supplementary material.

4.2.1. Human Variability Study

Twenty users with varying experience levels completed the testing protocol under controlled office conditions. Figure Fig. 8 shows the distribution of hand sizes (measured from the base of the wrist to tip of the middle finger) and skin tones among participants. Video recordings supplemented quantitative metrics to qualitatively analyse low-performing cases.

4.2.2. Scene Variability Study

An expert user conducted test sequences across four different home environments with only natural lighting. These included various floor textures, with light levels between 8-240 lux to test the model robustness.

4.2.3. Outdoor Performance Study

Group 2 participants from the human variability study repeated the same test sequence outdoors. Tests occurred

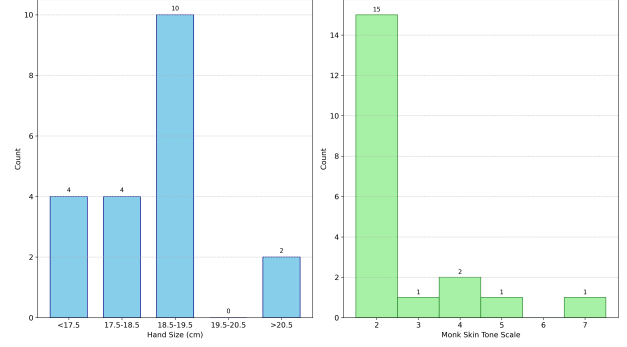


Figure 8. Histograms of user details. Left shows distribution of hand size and right shows distribution of skin tone based on the Monk Skin Tone Scale [34].

within a 30-minute window with consistent light levels of 3000 lux.

5. Methodology

5.1. Machine Learning Model

We developed a mobile-friendly ML architecture for microgesture detection optimised for low-power, low-latency performance on both CPU and DSP targets, making it suitable for always-on smart eyewear.

5.1.1. Model Architecture and Quantisation

Our five-stage model (Fig. 9) operates as follows:

- Stage 1: Downsamples the input time surface representation.
- Stage 2: Employs a CNN to predict hand bounding boxes with associated probability scores.
- Stage 3: Crops and resizes the original input using the predicted bounding box.
- Stage 4: Uses a separate CNN to predict microgesture probabilities.
- Stage 5: Combines stage 4 predictions with stage 2 hand-presence probabilities to produce final microgesture predictions.

The CNN components in stages 2 and 4 account for >99.8% of parameters and floating point operations. We quantised these stages to run on a Qualcomm Hexagon DSP, reducing power consumption and inference time. The final dense layers of these stages and the remaining three stages (which include interpolation and softmax functions) use 32-bit floating-point computation to maintain accuracy, as their minimal compute requirements make quantisation unnecessary.

We implemented QAT with 8-bit symmetric, per-channel weight quantisation and 8-bit asymmetric, per-tensor activation quantisation—a scheme natively supported by Hexagon DSP hardware that balances accuracy, latency, and power consumption. QAT is particularly important for our

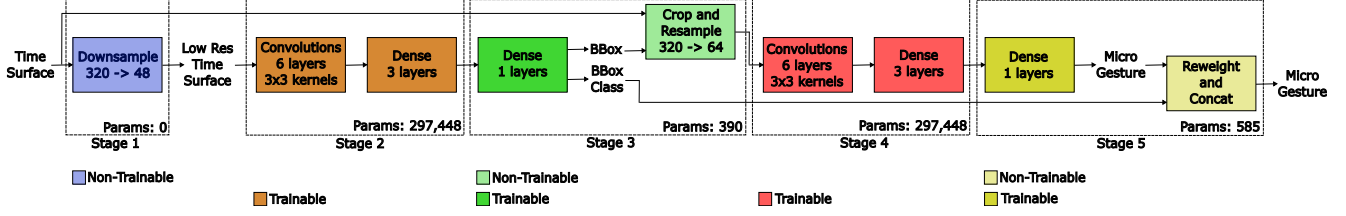


Figure 9. High-level block diagram of the five stage microgesture detection model architecture

parameter-constrained model to mitigate quantisation noise effects.

5.1.2. Training with Longer Sequences

A key contribution of our work is training the model (Sec. 5.1.1) with longer sequence datasets (Sec. 4.1.3). We aim to learn the conditional probability $p(g|\mathcal{I}_k)$ of predicting gesture class g given input \mathcal{I}_k , where \mathcal{I}_k is the LNES [45] representation for time-step k . Our datasets feature six distinct gestures within a 2 s sequence, each lasting ~ 333 ms. The construction of \mathcal{I}_k is detailed in Sec. 4.1.5. As outlined in Sec. 4.1.5 the simulator generates gesture labels at 900 Hz, yielding 216 labels per 240 ms window. To obtain g , the labels must be aggregated; in the case of the first sample in a sequence, we select the maximum across all 216 labels as g . Subsequently, we assign a new label only if its proportion exceeds the gesture threshold (e.g., at 0.6 threshold, a transition from ‘rest’ to ‘swipe right’ requires at least 60% of labels to be ‘swipe right’). This results in a corresponding g for each \mathcal{I}_k generated. We refer to these models as the 2-channels models.

To capture broader temporal context, we feed three consecutive TS samples ($\mathcal{I}_k, \mathcal{I}_{k-1}$, and \mathcal{I}_{k-2}) into the model, effectively capturing gestural evolution (e.g., a ‘swipe left’ should be followed by a ‘swipe left return’). Including positive and negative polarities, this representation has dimensionality $\{w, 6h\}$. We refer to these models as the 6-channels models.

5.2. Fine-tuning

To address the lack of rotation invariance in convolutional features, we augment our fine-tuning dataset with rotational variations. While the longer-sequence dataset (Sec. 4.1.3) captures diverse microgestures, it lacks comprehensive hand pose and orientation coverage. We apply uniform random rotations (25° - 40°) to each 2 s sequence, enhancing the model’s robustness to rotational variance. During fine-tuning, we freeze stages 1-3 and train only stages 4-5 with a reduced learning rate, preserving bounding-box localisation and low-level features while adapting to rotational variations.

5.3. Loss Function

Following [5], we employ two loss functions: $\mathcal{L}_{\text{bbox}}$, which calculates mean squared error between predicted and true bounding boxes (only when hands are present), and $\mathcal{L}_{\text{gesture}}$,

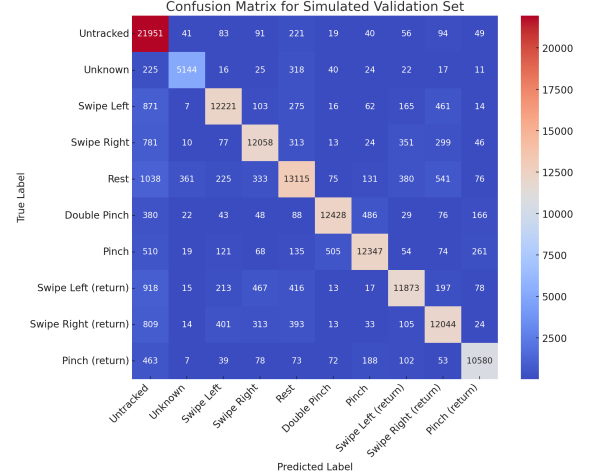


Figure 10. Confusion matrix for 2-channels TS QAT model trained from scratch on simulated validation set across 10 classes

a sparse categorical cross entropy loss for microgesture classification. $\mathcal{L}_{\text{bbox}}$ is essential because $\mathcal{L}_{\text{gesture}}$ alone cannot effectively guide hand centring in TS crops, and without it, the model initially focuses solely on distinguishing the no-hand class before learning other microgestures, leading to suboptimal performance due to local minima.

6. Experiments

We present results from our quantitative experiments, first evaluating our 2-channel low-power QAT model on simulated data (90% training, 10% validation). We render two versions of our longer sequences datasets: 1x and 4x. 1x has $\sim 25k$ training samples per microgesture class, while 4x has $\sim 100k$. We also apply the rotation augmentation as described in Sec. 5.2 on our 4x dataset to create a 4x Augmented dataset. We then assess both 2-channels and 6-channels models, across both CPU and DSP targets on real-world office environment data (Sec. 4.2.1). Following an ablation study of key model components in low-power quantized architectures, we evaluate the QAT models on scene-variability (Sec. 4.2.2) and outdoor datasets (Sec. 4.2.3). Using ground truth labels, we quantified TP, FP, and FN to calculate mean and median F1 scores across microgesture classes, alongside power consumption and latency measurements for both model configurations. For our experimental

Table 1. Comparison of Model Performance Across 2-channels and 6-channels models. All models are trained for 10 Epochs. Here RS stands for right swipe, LS is left swipe and CP is combined pinch. This is evaluated on the Human Variability Study Dataset.

Model	Type	Training Data	Mean F1 RS	Mean F1 LS	Mean F1 CP	Median F1 RS	Median F1 LS	Median F1 CP	Power (mW)	Latency (ms)
Helios [5]	CPU Model	-	0.6336	0.7314	0.5773	0.6826	0.8667	0.5965	350	60
2-channels TS	CPU Model	4x	0.7382	0.5229	0.7552	0.7214	0.5714	0.8568	144	6.15
	Fine-tuned CPU Model	4x Augmented	0.8081	0.8364	0.8572	0.9023	0.907	0.9505	144	6.15
	QAT Model	4x Augmented	0.8209	0.8244	0.8421	0.9045	0.8797	0.95	6	2.35
6-channels TS	CPU Model	4x	0.778	0.5477	0.7681	0.7625	0.6591	0.8739	172	7.46
	Fine-tuned CPU Model	4x Augmented	0.8512	0.8363	0.8429	0.9316	0.9115	0.9249	172	7.46
	QAT Model	4x Augmented	0.8149	0.8362	0.8902	0.9256	0.894	0.95	8	4.6

Table 2. Ablation of QAT model components. We use the 2-channels TS QAT model as our control model. This is evaluated on the Human Variability Study Dataset.

Model	Params, FLOPs	Mean F1 RS	Mean F1 LS	Mean F1 CP	Median F1 RS	Median F1 LS	Median F1 CP	Power (mW)
2-channels TS	596k, 164M	0.8209	0.8244	0.8421	0.9045	0.8797	0.95	6
Add 2 Dense layers in Stage 4	604k, 164M	0.7997	0.8032	0.8559	0.9094	0.8621	0.936	5
Replace Dense with Conv1D in Stages 1&3	605k, 165M	0.8232	0.8115	0.8675	0.9279	0.8752	0.95	5
Replace Conv2D with DepthwiseSeparable Conv2D in Stages 1&3	1.2M, 55M	0.7721	0.7988	0.7902	0.8971	0.8842	0.9744	6
Replace Conv2D with DepthwiseSeparable Conv2D in Stages 1&3 & strided-downsampling	391k, 25M	0.7624	0.6224	0.7365	0.8489	0.6559	0.9175	4
Replace Conv2D with DepthwiseSeparable Conv2D + Conv1D instead of Dense in Stages 1&3	113k, 24M	0.754	0.7817	0.7496	0.8514	0.8571	0.899	4
Replace Conv2D with DepthwiseSeparable Conv2D + Global Average Pooling (GAP) instead of Dense in Stages 1&3	70k, 52M	0.4054	0.2267	0.5466	0.2942	0.1765	0.6579	4
Replace Conv2D with DepthwiseSeparable Conv2D + Conv1D (stride=4) instead of Dense in Stages 1&3	86k, 53M	0.641	0.7003	0.7446	0.6667	0.809	0.8932	4

evaluation on real datasets, we report results on three microgesture classes - swipe right (RS), swipe left (LS) and combined pinch (CP, which is a combination of pinch and double-pinch classes).

6.1. Performance on Simulated Data

To evaluate our 2-channel low-power QAT model trained on simulated data, we analysed its confusion matrix across all 10 gesture classes (Fig. 10). The matrix’s diagonal dominance shows effective gesture discrimination, with minimal confusion between kinematically similar gestures (e.g., 2.8% between ‘swipe right (return)’ and ‘left swipe’). The model achieved 87.9% average class-wise precision, demonstrating successful feature learning despite quantisation constraints and readiness for real-world deployment.

6.2. User Testing for Human Variability

In this section, we present results on real-world test data collected as described in Sec. 4.2.1 to evaluate our model’s performance to human variability.

6.2.1. Helios CPU vs Helios 2.0 CPU vs Helios 2.0 DSP

In Fig. 11, we compare our CPU and QAT models against the Helios model presented in [5]. Given Helios is a CPU only model comparing our CPU model provides the most like for like comparison. This shows that our model improves the F1 score from 0.647 to 0.834 as well as reducing the power requirement from 350mW to 144mW, although it should be noted the CPU and memory architecture are different. As

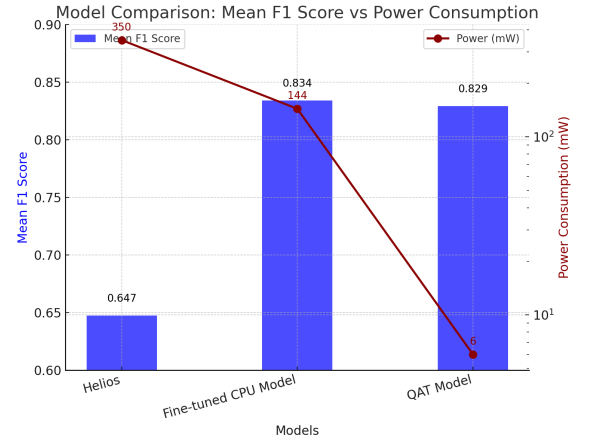


Figure 11. Mean F1 score across RS, LS and CP for user averages plotted against power consumption for Helios [5], our fine-tuned CPU model, and our QAT model

we designed our model such that two of the five stages (two and four) can be run on DSP we also compare to the QAT model. By quantizing those stages the F1 score reduces from 0.834 to 0.829, which is a minor reduction in performance, whilst reducing the power to 6mW. This means our model improves F1 score by 30% while only requiring 2.3% of the power.

6.2.2. Ablation Studies

Our ablation study (Tab. 1) shows that the TS models of 2-channels and 6-channels benefit from fine-tuning with rotation augmentation. This improvement occurs because

Table 3. Comparison of F1 Scores Across 2-channels and 6-channels QAT Models and 3 Real Datasets: User Variability, Outdoors and Scene Variability. All models are trained for 10 Epochs. Here RS stands for right swipe, LS is left swipe and CP is combined pinch.

Model	Real Dataset	Mean F1 RS	Mean F1 LS	Mean F1 CP	Median F1 RS	Median F1 LS	Median F1 CP
2-channels	User Variability (Group 2)	0.7365	0.7517	0.5439	0.8856	0.8558	0.4259
6-channels	User Variability (Group 2)	0.7806	0.754	0.71	0.918	0.8576	0.675
2-channels	Outdoors (Group 2)	0.8815	0.844	0.7084	0.898	0.9189	0.898
6-channels	Outdoors (Group 2)	0.9468	0.8309	0.8375	0.9499	0.8743	0.9744
2-channels	User Variability (User 3)	0.9744	0.9756	1	0.9744	0.9756	1
6-channels	User Variability (User 3)	0.9744	0.9756	1	0.9744	0.9756	1
2-channels	Scene Variability (User 3)	0.8702	0.7496	0.6962	0.8889	0.7242	0.7097
6-channels	Scene Variability (User 3)	0.8789	0.8436	0.8363	0.9041	0.8998	0.9189

the pre-training dataset, while useful for learning multiple micro-gesture sequences, lacks natural hand orientations. Fine-tuning helps the model adapt to realistic human hand distributions. While 6-channels TS input yields modest performance gains, it requires triple the data throughput, potentially increasing system power demands.

Tab. 2 compares various model modifications. Adding extra dense layers or replacing them with conv1D produced mixed results with minimal impact, suggesting small model capacity increases and layer type have limited effect on performance. Replacing conv2D with depthwise separable conv2D reduced FLOPs but showed inconsistent results, with decreasing mean F1 scores while slightly improving median scores. This indicates better performance for already well-served users at the expense of others. Other configurations (strided downsampling, depthwise separable conv2D with conv1D, global average pooling, and larger conv1D strides) all reduced both model size and performance, indicating a minimum capacity threshold required for effective micro-gesture learning.

6.3. User Testing for Environmental Variability

Performance comparison between User Variability and Outdoor datasets shown in Tab. 3 reveals consistent improvements in outdoor environments. The 2-channel TS model shows notable gains across all gestures outdoors, with Right Swipe improving from 0.7365 to 0.8815 (mean F1) and Combined-Pinch dramatically improving from 0.4259 to 0.898 (median F1). Similarly, the 6-channel TS model demonstrates enhanced outdoor performance, particularly for Right Swipe (0.7806 to 0.9468 mean F1) and Combined-Pinch (0.71 to 0.8375 mean F1, with median F1 jumping from 0.675 to 0.9744). These improvements show our quantised models not only maintain effectiveness in outdoor conditions but often perform better than controlled environments, likely due to stronger gesture signals against natural backgrounds and reduction in noise in brighter conditions.

6.4. User Testing for Scene Variability

Our analysis reveals a stark contrast between simple indoor office environments as used in the User Variability Dataset

and more complex environments used in the Scene Variability Dataset, as shown in Tab. 3. Both 2-channels and 6-channels models achieved identical, near-perfect scores in an office based environment (F1 scores of 0.97 for Right/Left Swipe and 1.0 for Combined-Pinch). However, introducing scene variability caused noticeable performance degradation, particularly for the 2-channel model, where Combined-Pinch recognition dropped from perfect scores to 0.6962 (mean F1). The 6-channels model demonstrated superior robustness to changing backgrounds, maintaining higher performance across all gestures and showing particularly significant advantages for Left Swipe (0.8436 vs. 0.7496 mean F1) and Combined-Pinch (0.8363 vs. 0.6962 mean F1). These results underscore the importance of background complexity in the training data. It also demonstrates that additional temporal information can help in difficult conditions.

7. Conclusion

In this paper, we propose Helios 2.0, a novel, ultra-low-power event-based vision system for intuitive hand gesture control in smart glasses. This addresses key challenges in power efficiency, adaptability, and user experience. Our system leverages a minimal set of microgestures that align with natural hand movements, making interactions more intuitive. By introducing an enhanced simulation methodology, a power-optimized model architecture, and comprehensive benchmarking, we achieve state-of-the-art F1 accuracy while operating at just 6-8 mW on a Qualcomm Snapdragon Hexagon DSP. These advancements significantly improve upon prior work, surpassing existing F1 scores by 20% while reducing power consumption by 25x. Our results are the first to comprehensively demonstrate that event-based vision can provide accurate, low-power, low-latency gesture recognition, making it an ideal solution for next-generation smart glasses.

In future work, we want to explore expanding the gesture vocabulary, improving adaptation to individual user preferences, and integrating multi-modal sensing for more robust interactions. As smart glasses continue to gain traction, our approach represents a critical step toward seamless, touch free human-computer interaction in wearable technology.

References

- [1] Manideep Reddy Aliminati, Bharatesh Chakravarthi, Aayush Atul Verma, Arpitsinh Vaghela, Hua Wei, Xuesong Zhou, and Yezhou Yang. Sevd: Synthetic event-based vision dataset for ego and fixed traffic perception. *arXiv preprint arXiv:2404.10540*, 2024. 2, 12
- [2] Arnon Amir, Brian Taba, David J. Berg, Timothy Melano, Jeffrey L. McKinstry, Carmelo di Nolfo, Tapan K. Nayak, Alexander Andreopoulos, Guillaume Garreau, Marcela Mendoza, Jeff Kusnitz, Michael DeBole, Steven K. Esser, Tobi Delbrück, Myron Flickner, and Dharmendra S. Modha. A low power, fully event-based gesture recognition system. In *2017 IEEE Conference on Computer Vision and Pattern Recognition, CVPR 2017, Honolulu, HI, USA, July 21-26, 2017*, pages 7388–7397. IEEE Computer Society, 2017. 2
- [3] Peijun Bao, Ana María Iglesias Maqueda, Carlos R. del Blanco, and Narciso García. Tiny hand gesture recognition without localization via a deep convolutional network. *IEEE Transactions on Consumer Electronics*, 63:251–257, 2017. 2
- [4] Gábor Berend. Efficient algorithm to compute markov transitional probabilities for a desired pagerank. *EPJ Data Science*, 9(1):23, 2020. 4
- [5] Prarthana Bhattacharyya, Joshua Mitton, Ryan Page, Owen Morgan, Ben Menzies, Gabriel Homewood, Kemi Jacobs, Paolo Baesso, David Trickett, Chris Mair, Taru Muhonen, Rory Clark, Louis Berridge, Richard Vigars, and Iain Wallace. Helios: An extremely low power event-based gesture recognition for always-on smart eyewear, 2024. 1, 2, 3, 4, 6, 7, 13
- [6] Yin Bi, Aaron Chadha, Alhabib Abbas, Eirina Boursoulatz, and Yiannis Andreopoulos. Graph-based object classification for neuromorphic vision sensing. In *2019 IEEE/CVF International Conference on Computer Vision, ICCV 2019, Seoul, Korea (South), October 27 - November 2, 2019*, pages 491–501. IEEE, 2019. 13
- [7] Christian Brandli, Raphael Berner, Minhao Yang, Shih-Chii Liu, and Tobi Delbruck. A 240×180 130 db $3 \mu\text{s}$ latency global shutter spatiotemporal vision sensor. *IEEE Journal of Solid-State Circuits*, 49:2333–2341, 2014. 12
- [8] Bharatesh Chakravarthi, Aayush Atul Verma, Kostas Daniilidis, Cornelia Fermuller, and Yezhou Yang. Recent event camera innovations: A survey, 2024. 12
- [9] Mahesh Chandra and Brejesh Lall. Low power gesture recognition system using skin statistics for consumer applications. *2016 IEEE International Conference on Consumer Electronics-Taiwan (ICCE-TW)*, pages 1–2, 2016. 2
- [10] Zhiwen Chen, Zhiyu Zhu, Yifan Zhang, Junhui Hou, Guangming Shi, and Jinjian Wu. Segment any event streams via weighted adaptation of pivotal tokens. In *Proceedings of the IEEE/CVF Conference on Computer Vision and Pattern Recognition*, pages 3890–3900, 2024. 12
- [11] Pierre de Tournemire, Davide Oscar Nitti, Etienne Perot, Davide Migliore, and Amos Sironi. A large scale event-based detection dataset for automotive. *ArXiv*, abs/2001.08499, 2020. 12
- [12] Laura Dipietro, Angelo Maria Sabatini, and Paolo Dario. A survey of glove-based systems and their applications. *IEEE Transactions on Systems, Man, and Cybernetics, Part C (Applications and Reviews)*, 38:461–482, 2008. 2
- [13] Guillermo Gallego, Tobi Delbrück, Garrick Orchard, Chiara Bartolozzi, Brian Taba, Andrea Censi, Stefan Leutenegger, Andrew J. Davison, Jörg Conradt, Kostas Daniilidis, and Davide Scaramuzza. Event-based vision: A survey. *IEEE Trans. Pattern Anal. Mach. Intell.*, 44(1):154–180, 2022. 2, 12, 13
- [14] Yuan Gao, Yuqing Zhu, Xinjun Li, Yimin Du, and Tianzhu Zhang. Sd2event: Self-supervised learning of dynamic detectors and contextual descriptors for event cameras. In *Proceedings of the IEEE/CVF Conference on Computer Vision and Pattern Recognition*, pages 3055–3064, 2024. 12
- [15] Mathias Gehrig, Willem Aarents, Daniel Gehrig, and Davide Scaramuzza. Dsec: A stereo event camera dataset for driving scenarios. *IEEE Robotics and Automation Letters*, 6:4947–4954, 2021. 12
- [16] Lin Guo, Lu Zongxing, and Ligang Yao. Human-machine interaction sensing technology based on hand gesture recognition: A review. *IEEE Transactions on Human-Machine Systems*, 51:300–309, 2021. 2
- [17] Benoit Jacob, Skirmantas Kligys, Bo Chen, Menglong Zhu, Matthew Tang, Andrew G. Howard, Hartwig Adam, and Dmitry Kalenichenko. Quantization and training of neural networks for efficient integer-arithmetic-only inference. *2018 IEEE/CVF Conference on Computer Vision and Pattern Recognition*, pages 2704–2713, 2017. 2
- [18] Shuiwang Ji, Wei Xu, Ming Yang, and Kai Yu. Ieee transactions on pattern analysis and machine intelligence 1 3d convolutional neural networks for human action recognition. 2
- [19] Damien Joubert, Alexandre Marcireau, Nicholas Ralph, A. Jolley, André van Schaik, and Gregory Cohen. Event camera simulator improvements via characterized parameters. *Frontiers in Neuroscience*, 15, 2021. 12
- [20] Junho Kim, Jaehyeok Bae, Gang-Ryeong Park, and Y. Kim. N-imagenet: Towards robust, fine-grained object recognition with event cameras. *2021 IEEE/CVF International Conference on Computer Vision (ICCV)*, pages 2126–2136, 2021. 12
- [21] Kenrick Kin, Chengde Wan, Ken Koh, Andrei Marin, Necati Cihan Camgöz, Yubo Zhang, Yujun Cai, Fedor Kovalev, Moshe Ben-Zacharia, Shannon Hoople, Marcos Nunes-Ueno, Mariel Sanchez-Rodriguez, Ayush Bhargava, Robert Wang, Eric Sauser, and Shugao Ma. STMG: A machine learning microgesture recognition system for supporting thumb-based VR/AR input. In *Proceedings of the CHI Conference on Human Factors in Computing Systems, CHI 2024, Honolulu, HI, USA, May 11-16, 2024*, pages 753:1–753:15. ACM, 2024. 2
- [22] Oscar Koller, Hermann Ney, and R. Bowden. Deep hand: How to train a cnn on 1 million hand images when your data is continuous and weakly labelled. *2016 IEEE Conference on Computer Vision and Pattern Recognition (CVPR)*, pages 3793–3802, 2016. 2
- [23] Lingdong Kong, Youquan Liu, Lai Xing Ng, Benoit R Cottureau, and Wei Tsang Ooi. Openess: Event-based semantic scene understanding with open vocabularies. In *Proceedings*

- of the *IEEE/CVF Conference on Computer Vision and Pattern Recognition*, pages 15686–15698, 2024. [12](#)
- [24] Mohidul Alam Laskar, Amlan Jyoti Das, Anjan Kumar Talukdar, and Kandarpa Kumar Sarma. Stereo vision-based hand gesture recognition under 3d environment. *Procedia Computer Science*, 58:194–201, 2015. [2](#)
- [25] Hongmin Li, Hanchao Liu, Xiangyang Ji, Guoqi Li, and Luping Shi. Cifar10-dvs: An event-stream dataset for object classification. *Frontiers in Neuroscience*, 11, 2017. [12](#)
- [26] Guoqiang Liang, Kanghao Chen, Hangyu Li, Yunfan Lu, and Lin Wang. Towards robust event-guided low-light image enhancement: A large-scale real-world event-image dataset and novel approach. In *Proceedings of the IEEE/CVF Conference on Computer Vision and Pattern Recognition*, pages 23–33, 2024. [12](#)
- [27] Songnan Lin, Ye Ma, Zhen-Qiang Guo, and Bihan Wen. Dvs-voltmeter: Stochastic process-based event simulator for dynamic vision sensors. In *European Conference on Computer Vision*, 2022. [12](#)
- [28] Baoyuan Liu, Min Wang, Hassan Foroosh, Marshall Tappen, and Marianna Pensky. Sparse convolutional neural networks. In *Proceedings of the IEEE conference on computer vision and pattern recognition*, pages 806–814, 2015. [12](#)
- [29] Fenglin Liu, Wei Zeng, Chengzhi Yuan, Qinghui Wang, and Ying Wang. Kinect-based hand gesture recognition using trajectory information, hand motion dynamics and neural networks. *Artificial Intelligence Review*, 52:563–583, 2019. [2](#)
- [30] John Jairo Villarejo Mayor, Regina M. Costa, Anselmo Frizera Neto, and Teodiano Bastos. Dexterous hand gestures recognition based on low-density semg signals for upper-limb forearm amputees. *Research on Biomedical Engineering*, 33: 202–217, 2017. [2](#)
- [31] Christen Millerdurai, Hiroyasu Akada, Jian Wang, Diogo Luizvizon, Christian Theobalt, and Vladislav Golyanik. Eventego3d: 3d human motion capture from egocentric event streams. In *Proceedings of the IEEE/CVF Conference on Computer Vision and Pattern Recognition*, pages 1186–1195, 2024. [12](#)
- [32] Pavlo Molchanov, Shalini Gupta, Kihwan Kim, and Jan Kautz. Hand gesture recognition with 3d convolutional neural networks. *2015 IEEE Conference on Computer Vision and Pattern Recognition Workshops (CVPRW)*, pages 1–7, 2015. [2](#)
- [33] Pavlo Molchanov, Xiaodong Yang, Shalini Gupta, Kihwan Kim, Stephen Tyree, and Jan Kautz. Online detection and classification of dynamic hand gestures with recurrent 3d convolutional neural networks. *2016 IEEE Conference on Computer Vision and Pattern Recognition (CVPR)*, pages 4207–4215, 2016. [2](#)
- [34] Ellis Monk. The monk skin tone scale, 2023. [5](#), [13](#)
- [35] Elias Mueggler, Henri Rebecq, Guillermo Gallego, Tobi Delbrück, and Davide Scaramuzza. The event-camera dataset and simulator: Event-based data for pose estimation, visual odometry, and slam. *The International Journal of Robotics Research*, 36:142 – 149, 2016. [12](#)
- [36] Markus Nagel, Marios Fournarakis, Rana Ali Amjad, Yelysei Bondarenko, Mart van Baalen, and Tijmen Blankevoort. A white paper on neural network quantization. *ArXiv*, abs/2106.08295, 2021. [2](#)
- [37] Natalia Neverova, Christian Wolf, Graham W. Taylor, and Florian Nebout. Multi-scale deep learning for gesture detection and localization. In *ECCV Workshops*, 2014. [2](#)
- [38] G. Orchard, Ajinkya Jayawant, Gregory Cohen, and Nitish V. Thakor. Converting static image datasets to spiking neuro-morphic datasets using saccades. *Frontiers in Neuroscience*, 9, 2015. [12](#)
- [39] Yansong Peng, Hebei Li, Yueyi Zhang, Xiaoyan Sun, and Feng Wu. Scene adaptive sparse transformer for event-based object detection. In *Proceedings of the IEEE/CVF Conference on Computer Vision and Pattern Recognition*, pages 16794–16804, 2024. [12](#)
- [40] Etienne Perot, Pierre de Tournemire, Davide Nitti, Jonathan Masci, and Amos Sironi. Learning to detect objects with a 1 megapixel event camera. In *Advances in Neural Information Processing Systems 33: Annual Conference on Neural Information Processing Systems 2020, NeurIPS 2020, December 6-12, 2020, virtual*, 2020. [12](#)
- [41] P. PramodKumar and Martin Saerbeck. Recent methods and databases in vision-based hand gesture recognition: A review. *Comput. Vis. Image Underst.*, 141:152–165, 2015. [2](#)
- [42] Henri Rebecq, Daniel Gehrig, and Davide Scaramuzza. ESIM: an open event camera simulator. In *2nd Annual Conference on Robot Learning, CoRL 2018, Zürich, Switzerland, 29-31 October 2018, Proceedings*, pages 969–982. PMLR, 2018. [3](#), [4](#), [12](#)
- [43] Henri Rebecq, René Ranftl, Vladlen Koltun, and Davide Scaramuzza. Events-to-video: Bringing modern computer vision to event cameras. In *IEEE Conference on Computer Vision and Pattern Recognition, CVPR 2019, Long Beach, CA, USA, June 16-20, 2019*, pages 3857–3866. Computer Vision Foundation / IEEE, 2019. [12](#)
- [44] Hongwei Ren, Jiadong Zhu, Yue Zhou, Haotian Fu, Yulong Huang, and Bojun Cheng. A simple and effective point-based network for event camera 6-dofs pose relocation. In *Proceedings of the IEEE/CVF Conference on Computer Vision and Pattern Recognition*, pages 18112–18121, 2024. [12](#)
- [45] Viktor Rudnev, Vladislav Golyanik, Jiayi Wang, Hans-Peter Seidel, Franziska Mueller, Mohamed Elgharib, and Christian Theobalt. Eventhands: Real-time neural 3d hand pose estimation from an event stream. In *Proceedings of the IEEE/CVF international conference on computer vision*, pages 12385–12395, 2021. [4](#), [6](#), [13](#)
- [46] Simon Schaefer, Daniel Gehrig, and Davide Scaramuzza. AEGNN: asynchronous event-based graph neural networks. In *IEEE/CVF Conference on Computer Vision and Pattern Recognition, CVPR 2022, New Orleans, LA, USA, June 18-24, 2022*, pages 12361–12371. IEEE, 2022. [12](#), [13](#)
- [47] Yuzhang Shang, Zhihang Yuan, Bin Xie, Bingzhe Wu, and Yan Yan. Post-training quantization on diffusion models. *2023 IEEE/CVF Conference on Computer Vision and Pattern Recognition (CVPR)*, pages 1972–1981, 2022. [2](#)
- [48] Abhik Singla, Partha Pratim Roy, and Debi Prosad Dogra. Visual rendering of shapes on 2d display devices guided by hand gestures. *ArXiv*, abs/1810.10581, 2018. [2](#)

- [49] Ayan Sinha, Chiho Choi, and Karthik Ramani. Deephand: Robust hand pose estimation by completing a matrix imputed with deep features. *2016 IEEE Conference on Computer Vision and Pattern Recognition (CVPR)*, pages 4150–4158, 2016. 2
- [50] Amos Sironi, Manuele Brambilla, Nicolas Bourdis, Xavier Lagorce, and Ryad B. Benosman. Hats: Histograms of averaged time surfaces for robust event-based object classification. *2018 IEEE/CVF Conference on Computer Vision and Pattern Recognition*, pages 1731–1740, 2018. 12, 13
- [51] Ganchao Tan, Yang Wang, Han Han, Yang Cao, Feng Wu, and Zhengjun Zha. Multi-grained spatio-temporal features perceived network for event-based lip-reading. *2022 IEEE/CVF Conference on Computer Vision and Pattern Recognition (CVPR)*, pages 20062–20071, 2022. 12
- [52] Senmao Tian, Haoyu Gao, Gangyi Hong, Shuyun Wang, Jingjie Wang, Xin Yu, and Shunli Zhang. Qgait: Toward accurate quantization for gait recognition with binarized input. *ArXiv*, abs/2405.13859, 2024. 2
- [53] Ultraleap Inc. Orion hand tracking software. 3
- [54] Unity Technologies. Unity engine. 3
- [55] Aayush Atul Verma, Bharatesh Chakravarthi, Arpitsinh Vaghela, Hua Wei, and Yezhou Yang. etram: Event-based traffic monitoring dataset. *2024 IEEE/CVF Conference on Computer Vision and Pattern Recognition (CVPR)*, pages 22637–22646, 2024. 12
- [56] Xiao Wang, Shiao Wang, Chuanming Tang, Lin Zhu, Bowei Jiang, Yonghong Tian, and Jin Tang. Event stream-based visual object tracking: A high-resolution benchmark dataset and a novel baseline. *2024 IEEE/CVF Conference on Computer Vision and Pattern Recognition (CVPR)*, pages 19248–19257, 2023. 12
- [57] Wikipedia. List of Qualcomm Snapdragon systems on chips — Wikipedia, the free encyclopedia. <http://en.wikipedia.org/w/index.php?title=List%20of%20Qualcomm%20Snapdragon%20systems%20on%20chips&oldid=1278216463>, 2025. [Online; accessed 07-March-2025]. 3
- [58] Hao Wu, Patrick Judd, Xiaojie Zhang, Mikhail Isaev, and Paulius Micikevicius. Integer quantization for deep learning inference: Principles and empirical evaluation. *ArXiv*, abs/2004.09602, 2020. 2
- [59] Wei Xia, Linwei Ye, and Honghai Liu. A gesture database of b-mode ultrasound-based human-machine interface. *2017 International Conference on Machine Learning and Cybernetics (ICMLC)*, 1:118–122, 2017. 2
- [60] Bohan Yu, Jieji Ren, Jin Han, Feishi Wang, Jinxiu Liang, and Boxin Shi. Eventps: Real-time photometric stereo using an event camera. In *Proceedings of the IEEE/CVF Conference on Computer Vision and Pattern Recognition*, pages 9602–9611, 2024. 12
- [61] Wei Zeng, Cong Wang, and Qinghui Wang. Hand gesture recognition using leap motion via deterministic learning. *Multimedia Tools and Applications*, 77:28185 – 28206, 2018. 2
- [62] Baoheng Zhang, Yizhao Gao, Jingyuan Li, and Hayden Kwok-Hay So. Co-designing a sub-millisecond latency event-based eye tracking system with submanifold sparse cnn. In *Proceedings of the IEEE/CVF Conference on Computer Vision and Pattern Recognition*, pages 5771–5779, 2024. 12
- [63] Hanyu Zhou, Yi Chang, Zhiwei Shi, and Luxin Yan. Bring event into rgb and lidar: Hierarchical visual-motion fusion for scene flow. *2024 IEEE/CVF Conference on Computer Vision and Pattern Recognition (CVPR)*, pages 26467–26476, 2024. 12
- [64] Jiazhou Zhou, Xueye Zheng, Yuanhuiyi Lyu, and Lin Wang. Exact: Language-guided conceptual reasoning and uncertainty estimation for event-based action recognition and more. *2024 IEEE/CVF Conference on Computer Vision and Pattern Recognition (CVPR)*, pages 18633–18643, 2024. 12

A. Extension of Related Work

The following sections give some more details of prior work in the field of event based vision.

A.1. Event Camera Datasets and Simulators

Event sensors offer unprecedented temporal resolution while operating at extremely low power levels, as low as 3 mW. In contrast, traditional frame-based sensors require a trade-off between temporal resolution and power consumption, typically ranging from 35 to 200 mW, depending on the frame rate. Event cameras operate on an asynchronous, per-pixel sensing mechanism, fundamentally different from conventional frame-based cameras [13]. It is inspired by the human retina where each pixel functions independently, continuously detecting changes in light intensity.

When the intensity at a event camera pixel surpasses a pre-defined threshold, the sensor records an event in the form of $\langle x, y, t, p \rangle$, where (x, y) represent the pixel coordinates, t is the event timestamp, and $p \in \{1, -1\}$ indicates whether the light intensity increased or decreased.

While conventional machine vision architectures are optimised for frame-based data, they struggle to meet the demands of wearable and low-power applications, driving the need for event-based vision research. This section provides an overview of the current landscape of event camera datasets and simulators, which are essential for developing and training event-driven machine learning algorithms.

A.2. Event Camera Datasets: Real and Synthetic

Real-world datasets, captured using event cameras such as DAVIS [7] and Prophesee, cover diverse applications like object detection, action recognition, tracking, and 3D perception. Datasets like EventVOT [56] and eTraM [55] focus on object tracking and traffic monitoring, while DVS-Lip [51] and SeAct [64] explore fine-grained human motion and action recognition.

Automotive datasets such as DSEC [15], GEN1 [11], 1 MPX [40] and N-Cars [50] provide event streams for autonomous driving. However, real-world datasets are constrained by hardware limitations, environmental conditions, and annotation challenges, making it difficult to scale data collection efficiently. To address these gaps, synthetic datasets leverage simulators to generate large-scale, controlled event streams. For example, Event-KITTI [63] extends the popular KITTI dataset with event-based representations. Datasets such as N-ImageNet [20], CIFAR10-DVS [25], and N-MNIST [38] convert standard image datasets into event streams, enabling model benchmarking across classification tasks. Despite these advances, synthetic datasets often lack realistic noise characteristics, which can impact generalisation to real-world scenarios.

In this work, we propose the development of a specialised event-based simulator to generate microgesture data tailored

to our specific application. This approach is motivated by the absence of both real-world and synthetic datasets that sufficiently address our requirements. By leveraging simulation, we can precisely control gesture variations, environmental conditions, and sensor parameters, enabling the creation of high-fidelity data that aligns with our use case. We also detail three datasets collected from internal studies, covering user variability, where environment was fixed, environment variability, with a single expert user across ambient lit complex scenes and an outdoor dataset utilising one of the groups from the user variability study. These provide benchmarks for key areas needed to access a system targeting smart-eyewear.

A.3. Event Camera Simulators

A review of recent event simulators can be found in [8]. Notable simulators include the DAVIS Simulator [35], which generated event streams, intensity frames, and depth maps with high temporal precision through time interpolation. ESIM [42] extends this by modelling camera motion in 3D environments. Unlike traditional frame-based simulators, ESIM accurately simulates the asynchronous nature of event cameras, ensuring that events are generated only when intensity changes occur. More advanced simulators like ICNS Simulator [19] introduce realistic noise models improving the fidelity of synthetic events, while DVS-Voltmeter [27] incorporates stochastic variations in sensor behaviour.

Simulators like ESIM are not inherently designed for human-centric applications, such as gesture recognition. To address this limitation, we leverage the work of ESIM alongside our custom rendering engine, developed in Unity, to generate synthetic event data of hands performing microgestures.

A.4. ML for Event Vision

ML approaches for event-based classification and detection typically transform raw event data into structured representations, such as time surfaces or event volumes, which can then be processed using standard Convolutional Neural Networks (CNNs) or recurrent architectures like Conv-LSTMs [1, 10, 14, 23, 26, 31, 43]. While these methods are straightforward to implement, they introduce redundant computations and can be computationally expensive due to the dense processing of inherently sparse data. To overcome these inefficiencies, researchers have explored sparse convolutional architectures [28] which compute convolutions only at active sites with non-zero feature vectors, significantly reducing computational overhead [39, 60, 62]. Additionally, techniques leveraging temporal sparsity aim to retain previous activations and apply recursive sparse updates [44, 46], rather than reprocessing the entire event volume. Beyond grid-based representations, graph-based methods maintain the compact, asynchronous structure of event



Figure 12. The Monk Skin Tone Scale, with corresponding numbering from 1 light to 10 dark.

streams, with Graph Neural Networks (GNNs) providing an efficient framework for handling irregular and dynamic event data [6, 46].

A.5. Event Representations

Two widely used representations of event data for machine learning applications are time surfaces and event volumes [13]. Time surfaces store the timestamp of the most recent event for each pixel and polarity, forming a 2D map where each pixel retains a single time value. This compact representation efficiently encodes temporal dynamics but becomes less effective in textured scenes where pixels generate frequent events. By aggregating local memory time surfaces, Histograms of Averaged Time Surfaces (HATS) [50] construct a higher-order representation to improve temporal and noise robustness.

In contrast, event volumes represent events as 3D histograms, maintaining richer temporal structure by accumulating events over time. While event volumes provide a more detailed temporal representation, they may lose polarity information due to voxel-based accumulation, potentially reducing their effectiveness in tasks requiring fine-grained contrast changes.

In our work, we employ polarity-separated time surfaces [45] as our event representation to achieve both computational and storage efficiency. By separating polarities, we mitigate event clashes and ensure a more structured and accurate representation of the temporal dynamics in event data.

B. Additional Background for Real Dataset Creation

The datasets created using internal users utilised the Monk Skin Tone Scale [34], an illustration of the scale is shown in Fig. 12. Using this scale enables a qualitative way to assess coverage of benchmark datasets. Ensuring as we expand the datasets we ensure equal representation.

In the User Variability Dataset the user was asked to stand within a square and were oriented using an arrow marked on

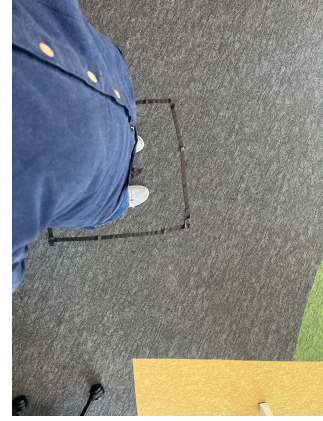


Figure 13. Image showing background used for user studies, along with floor marking to ensure minimal background variability between users. Lighting was measured at 60 lux.

the floor. This ensured that between users the background did not change, an RGB image from the view point of the event camera is shown in Fig. 13 illustrating the background used.

To test across more challenging environments, the Scene Variability Dataset was created. This consists of different floor textures, with varying light levels. An RGB image for each is shown in Fig. 14, illustrating the variation in backgrounds used.

In the final dataset we consider an outdoor scene, a RGB reference image is shown in Fig. 15.

C. Training Parametrisation and Inference Details

We trained the network for 10 epochs with a batch size of 512. We use the Adam optimiser with an initial learning rate of 0.0005. We utilise a learning rate scheduler, which linearly decays the learning rate after an initial period where the learning rate is held fixed. We apply dropout with 0.2 drop rate on the dense layers and set the gesture threshold value to 0.6.

At inference time the model takes as input TS of window size 240 ms. To avoid sampling issues we follow the approach of [5] and create an TS every 80 ms. This follows the intuition that the model will be less confident on predictions where non-complete microgestures have occurred in the input frame. The model will therefore predict a microgesture with a larger probability when a complete microgesture has occurred and a lower probability when a non-complete microgesture has occurred. We also overcome the issue of the model predicting a microgesture with low confidence by introducing a threshold on softmax probabilities, at which a microgesture is deemed to have occurred, and set it to 0.65.



Figure 14. Various backgrounds with natural illumination measured at the event camera position: (a) 8 lux, (b) 140 lux, (c) 30 lux, (d) 240 lux.



Figure 15. Outdoor scene showing hand in foreground with paving stones as a background. Ambient light= 3000 lux.

D. Additional Results

The following sections give details on some additional results, covering training schemes and variability and visualisation of feature embeddings.

D.1. Training Strategies

Tab. 4 shows the impact of different training strategies. Based on the mean F1 scores across all three metrics we find that the training from scratch and from 4x fine-tuned 4x base

model perform the strongest, with both of these models scoring above 0.8 F1 score across all micro-gestures. When considering the median scores the from 4x fine-tuned 4x base model achieves the highest average F1 score across all three micro-gestures.

D.2. QAT Model Performance and Seed Variability

We analyse seed variability using standard deviation σ as an error measure. We compute σ across five independent runs for both mean and median F1 scores. Seed variability for QAT models is a crucial factor in assessing its generalisability beyond a single training instance. We observe that mean F1 scores exhibit larger error bars. In contrast, median F1 scores have smaller error bars, suggesting that the model performs consistently well in most runs. CP exhibits the lowest median variability ($\sigma = 0.005$), making it the most stable gesture. LS follows with slightly higher median variability ($\sigma = 0.010$), while RS demonstrates the highest fluctuation ($\sigma = 0.015$). The contrast between CP and RS highlights a difference in recognition stability - the robust classification performance of CP remains stable throughout the tests, while RS exhibits greater sensitivity to specific seed initialisations.

D.3. t-SNE Visualisation of Learned Feature Embeddings

Fig. 17 illustrates the t-SNE visualisation of our 2-channels QAT model's learned feature embeddings from the dense layer in Stage 4, across the 10 microgesture classes. The visualisation reveals distinct clustering patterns for each gesture type, demonstrating the model's ability to learn discriminative representations despite the quantisation constraints. Interestingly, directional gestures such as 'Left', 'Right', 'Left Return', and 'Right Return' form well-separated clusters with clear trajectory patterns. Also, 'Pinch', 'Double Pinch', and 'Pinch Return' classes show structured separation with minimal overlap. The 'Rest' class manifests as a cluster with moderate dispersion. Particularly interesting is

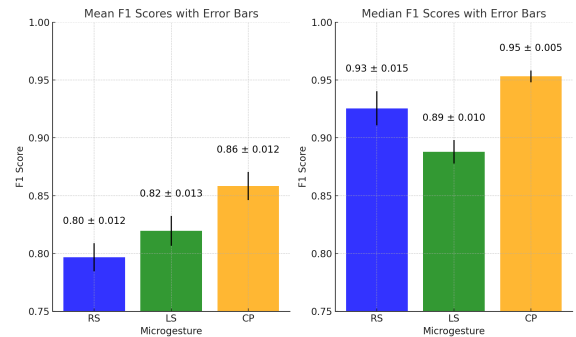


Figure 16. Mean and Median F1 Scores with Error Bars across 5 seeds for microgestures right swipe(RS), left swipe(LS), and combined pinch(CP) for training 2-channels TS QAT models

Table 4. Impact of different training strategies for Quantization-aware training (QAT). Here RS stands for right swipe, LS is left swipe and CP is combined pinch.

Training Strategy	Training Stages	Epochs	Training Data	Mean F1 RS	Mean F1 LS	Mean F1 CP	Median F1 RS	Median F1 LS	Median F1 CP
From scratch	QAT	10	4x Augmented	0.8209	0.8244	0.8421	0.9045	0.8797	0.95
From 1x Base Model	Base model QAT	10 5	1x 4x Augmented	0.7771	0.8127	0.8638	0.9237	0.8896	0.9629
From 4x Fine-tuned 1x Base Model	Base model Fine-tuned QAT	10 5 5	1x 4x Augmented 4x Augmented	0.7699	0.8342	0.8496	0.906	0.9034	0.9744
From 4x Fine-tuned 4x Base Model	Base model Fine-tuned QAT	10 5 5	4x 4x Augmented 4x Augmented	0.8189	0.8033	0.8571	0.9379	0.8782	1.0000

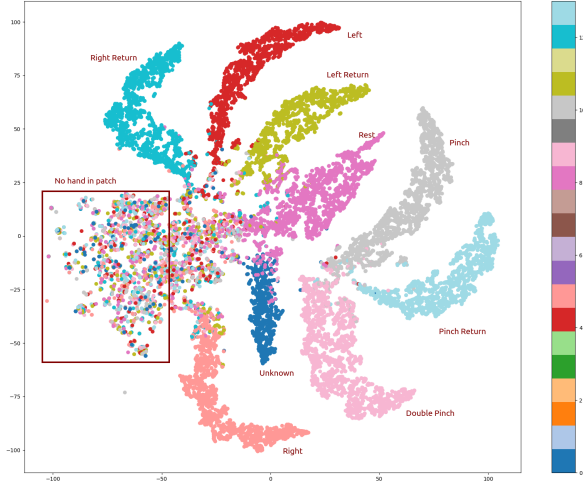


Figure 17. TSNE for 2-channels TS Fine-tuned CPU model across 10 classes

the ‘No hand in patch’ region (highlighted by the red box), which shows a mixed distribution of points, indicating the model’s uncertainty when no clear hand features are present. The ‘Unknown’ class forms a concentrated cluster, suggesting consistent identification of ambiguous hand motions. This embedding structure provides visual evidence of the model’s strong feature extraction capabilities, which directly contributes to the classification performance observed in our quantitative evaluations.